Effect of implanted argon on hardness of novel magnetron sputtered Si–B–C–N materials: experiments and *ab initio* simulations

2007 J. Phys.: Condens. Matter 19 196228

(http://iopscience.iop.org/0953-8984/19/19/196228)

IOP Publishing Journal of Physics: Condensed Matter

J. Phys.: Condens. Matter **19** (2007) 196228 (13pp) doi:10.1088/0953-8984/19/19/196228

Effect of implanted argon on hardness of novel magnetron sputtered Si–B–C–N materials: experiments and *ab initio* simulations

J Houška[1], J Kalaš[1], J Vlček[1], M M M Bilek[2] and D R McKenzie[2]

[1] Department of Physics, University of West Bohemia, Univerzitni 22, 30614 Plzen, Czech Republic
[2] School of Physics, The University of Sydney, Sydney, NSW 2006, Australia

E-mail: jhouska@kfy.zcu.cz

Received 8 March 2007, in final form 2 April 2007
Published 26 April 2007
Online at stacks.iop.org/JPhysCM/19/196228

Abstract

Amorphous silicon–boron–carbon–nitrogen alloys were deposited by reactive magnetron sputtering in nitrogen–argon gas mixtures, and their structure and resulting mechanical properties were investigated using a combined approach of experiment and molecular-dynamics simulations. We show a difference between structures of the materials deposited with a low substrate bias voltage of −100 V leading to a 2% content of implanted Ar atoms, and a high substrate bias voltage of −500 V, resulting in a 6% content of implanted Ar atoms. We find that, while at the higher Ar content the material is practically homogeneous, at the low Ar content there are similar volumes of Si-rich (around the implanted Ar atoms) and Si-poor zones. This can increase material hardness. We examine a temperature dependence of this phenomenon in the light of experimental results.

1. Introduction

Amorphous Si–B–C–N materials are of increasing interest due to their combination of exceptional high-temperature stability, oxidation resistance and creep resistance at elevated temperatures with superior mechanical, optical and electrical properties. In particular, materials have been reported that feature one or more of thermal stability in an inert atmosphere up to 1900–2000 °C [1–3], oxidation resistance up to 1300–1500 °C [4, 5], hardness up to 47 GPa [5] at compressive stress below 1.6 GPa [5], transparency in visible spectra or controllable electrical conductivity [6] significantly higher than for the Si–C–N ceramics [7]. This unique combination of properties leads to many potential applications in areas such as coating technologies [8, 9], microelectronics [7, 9] or production of thermally stable fibres for composites [10].

The effect of the N_2–Ar discharge gas mixture composition [5, 11] and of the negative substrate bias voltage [6] on mechanical properties of the Si–B–C–N materials (with a small content of implanted Ar atoms) prepared by reactive magnetron sputtering has been recently studied experimentally. Both these process parameters affect content of the implanted Ar in materials, at only minor changes in contents of Si, B, C and N. The effect of Ar on the structure of Si–B–C–N networks has been investigated in our previous paper [12]. However, there is no information about the complex relationships between process parameters, the Ar content, atomic-scale structure of the Ar-containing Si–B–C–N networks and material hardness. molecular-dynamics(MD) simulations are a suitable technique for investigating such phenomena, confirming and explaining experimental results and obtaining information which is not accessible experimentally [13, 14].

The aim of this study is twofold. First, we investigate the effect of the substrate bias voltage, U_b, on averaged material characteristics which are known to affect the bulk modulus (and therefore hardness), such as the coordination number, bond length and bond ionicity. The results show that differences in these quantities cannot explain the experimentally observed large differences in material hardness. Second, we introduce and examine the idea that a proper content of the implanted Ar leads to an increased hardness due to a thermally activated replacement of a homogeneous material structure by a heterogeneous mixture of Si-rich (around the Ar atoms) and Si-poor zones. The prediction is tested against several experimental results, such as differences between the dependencies of hardness on the sputter target composition measured at two different substrate temperatures, differences between the dependencies of hardness on the discharge gas mixture composition obtained for two different U_b values and a temperature dependence of an hardness increase after annealing of the deposited materials in helium.

2. Experimental details and methodology

2.1. Film preparation and characterization

Si–B–C–N samples studied in this work were produced in the form of films (2–5 μm thick) using reactive magnetron sputtering. Advantages of this versatile technique, compatible with semiconductor technologies, include low process temperatures, controllably low H content due to absence of H-containing precursors and an easy up-scaling.

The Si–B–C–N films were deposited on p-type Si(100) substrates using dc magnetron co-sputtering of silicon, boron and carbon in N_2–Ar mixtures from a C–Si–B (a graphite plate overlapped by p-type Si and B stripes) or B_4C–Si (a B_4C plate overlapped by p-type Si stripes) composite targets, with a negative bias voltage, U_b, applied to substrates at the temperature, T_s. The Si fraction in the target erosion area was varied from 5 to 75% at a fixed 20% B fraction for the C–Si–B target, while it ranged from 0 to 75% for the B_4C–Si target. The Ar content in the N_2–Ar gas mixture composition was up to 75% at a gas flow approximately 25 sccm and a total pressure of 0.5 Pa. The negative substrate bias voltage, U_b, varied from a floating potential of -15 to -500 V, was induced (except the floating potential) by an rf generator operating at a frequency of 13.56 MHz and was measured using a respective unit built into the generator. The substrate temperature, T_s, was adjusted up to 700 °C by an ohmic heater or it was $\leqslant$250 °C without the heater. The target-to-substrate distance was 100 mm and the discharge current on the magnetron target, I_m, was held constant at 1 A. The experimental set-up is described in detail in [5].

The atomic concentrations of Si, B, C, N and Ar in the films were determined by Rutherford back-scattering spectroscopy (RBS) as described in detail in [5]. In selected cases,

the boron content was determined using neutron depth profiling. The atomic density of the films was determined using the number of film atoms per cm^2 (measured by RBS) divided by the film thickness (given by profilometry). The surface atomic densities of the deposited films were around 1.0×10^{19} atoms cm^{-2} per 1 μm of the film thickness. This leads to the volume atomic densities (used in the simulations) close to 100 atoms nm^{-3}.

Film hardness was determined using a computer-controlled microhardness tester (Fischerscope H-100B) which automatically records the depth of indentation of a Vickers diamond pyramidal tip, while increasing the applied load up to a preset maximum. The plastic hardness was calculated from the indentation depth after unloading, and it was corrected for the indentation size effect. The results are shown for a maximum load of 30 mN (see similar results and the same trends of the values measured on these materials with a maximum load of 50 mN in [5, 6, 11]).

2.2. Ab initio calculations

All the calculations reported in this work use the density functional theory (DFT) [15, 16] as implemented in the Car–Parrinello molecular dynamics (CPMD) code [17]. Atom cores and inner electron shells were represented by the Goedecker-type pseudopotentials [18]. Valence electrons were described using the Kohn–Sham equations solved in the generalized-gradient approximation (GGA, BLYP functional [19, 20]) and their wavefunction was expanded using a plane-wave basis set with an energy cut-off of 60 Ryd. The accuracy of this method, as well as the convergence of calculated properties with respect to the plane-wave cut-off has been confirmed previously [21]. All MD runs were performed using a time step of 0.073 fs and the fictitious electron mass (required for a classical integration of the electronic degrees of freedom) was set to 200 m_e. A temperature control was achieved by the Nose–Hoover thermostats (electrons and ions during the constant-temperature MD runs) and by a velocity scaling when the simulation and target temperature differed by more than 10% (ions during varied-temperature MD runs, i.e. cooling).

In our simulation work, we try to describe the formation process of Si–B–C–N materials using a liquid-quench algorithm. This algorithm captures the formation conditions of real materials, which arise from a rapid cooling of the localized melt created around sites of energetic ion impacts. Using presently available quantum theoretical methods it is not possible to simulate the full ion bombardment process. Therefore we simplify the process by assuming that the primary impact creates a localized region of high temperature, commonly referred to as a *thermal spike*. The thermal spikes have a cooling time sufficiently short to be simulated using *ab initio* MD methods, as shown in [22]. The thermal spike simulation method has been used successfully to predict structure of carbon materials formed from ion beams having a range of energies [23].

The algorithm includes (1) generating of starting structure—periodical cubic cell with 100 atoms of the experimental atomic density and elemental composition (plus an N excess necessary due to the formation of free N_2 molecules during the simulation [21]), (2) an initial mixing of a molten phase (>5000 K) for 1 ps in order to forget the initial configuration, (3) a N_2 removal run at 4000–5000 K, which ends when the number of network N atoms (i.e. without those which formed free N_2 molecules or almost-free triple bonded N–N pairs) is equal to the desired N content, (4) an exponential cooling from 3000 K (when the N_2 formation ends) to the deposition temperature for up to 0.5 ps, (5) an equilibration at the deposition temperature for 1 ps, and finally (6) collecting all characteristics of the structure for 0.5 ps at the deposition temperature. During the simulation, the N_2 molecules formed (which cannot diffuse out, as in the real material, according to the periodic boundary conditions) are manually removed,

which is followed by a rescaling of the simulation cell in order to keep the atomic density constant.

Liquid quench simulations were performed for the compositions $Si_{31}B_8C_9N_{46}Ar_6$ (deposited at $U_b = -500$ V) and $Si_{31}B_8C_{13}N_{46}Ar_2$ ($U_b = -100$ V), representing similar materials prepared with the same sputter target and different substrate bias voltage, U_b. The temperature dependence of the hardness increase was examined for the composition $Si_{32}B_{10}C_6N_{52}Ar_6$.

3. Results and discussion

3.1. Ab initio simulations

3.1.1. Structural quantities. Typical Si–B–C–N structures obtained at the end of the exponential cooling and subsequent equilibration runs with the composition $Si_{31}B_8C_{13}N_{46}Ar_2$ at a cooling time of 100 fs and with the composition $Si_{31}B_8C_9N_{46}Ar_6$ at a cooling time of 500 fs are shown in figure 1. The cooling time of 100 fs was used to simulate the ion bombardment effects at $U_b = -100$ V, leading to a 2% content of Ar atoms in the material. The cooling time of 500 fs simulated these effects at $U_b = -500$ V, when the Ar content in the material increased to 6 at.% and the C content decreased due to a stronger resputtering of loosely bounded C–N compounds [5, 24]. In figure 1, pairs of valence electrons are represented by the Wannier function centres (WFCs) [25]—the small black dots—as described in [14]. A WFC can represent a lone pair if it is associated with one atom, or a bonding electron pair (single bond or a part of a multiple bond) if it is associated with two atoms. The Ar atoms can be seen as isolated balls sitting in cavities, with all four WFCs (i.e. eight valence electrons) close to them. As described previously [12], the Ar implantation into Si–B–C–N materials leads to a formation of silicon-enriched zones around implanted Ar atoms. The energy advantage gained by surrounding the large Ar-containing cavities with longer and more flexible Si-containing bonds was proposed to be a driving force for this segregation. This leads to a formation of a sort of two-phase material, consisting of amorphous Si-rich (close-to-Ar) and Si-poor (far-from-Ar) regions. The described accommodating of the Ar atoms into the structure with minimal energy penalty has been correlated with the experimentally known ability of Si to inhibit the extra stress, otherwise generated by implanted Ar in (Si)–B–C–N materials with zero or low Si content.

In 1985, Cohen published the following empirical formula [26] which describes very well the dependence of the bulk modulus B_m on the averaged coordination number, N_c, bond length, a_0 and bond ionicity, λ:

$$B_m = \frac{N_c}{4}(1971 - 220\lambda)a_0^{-3.5}.$$

Although the formula was primarily derived for crystalline materials, qualitative predictions based on differences in N_c, a_0 and λ can also be made for amorphous materials. While N_c and a_0 can be directly calculated from the simulated network structures, λ is to be derived from positions of the Wannier function centres, which define the bonds.

We simulated networks of several known crystalline materials containing elements from the IVA group (cubic and wurtzite SiC) and IIIA + VA group (cubic and wurtzite BN, cubic AlP and wurtzite AlN), and observed the quantity $\Lambda = d_1r_2/d_2r_1$—see table 1. Here, $d_{1(2)}$ are the distances of the first (second) atom from the Wannier centre defining the bond between them, and $r_{1(2)}$ are the covalent radii of the atoms. In order to calculate the bond ionicity, λ, we use a simple linear relation between λ and Λ: $\lambda = (\Lambda - 1)/(\Lambda_0 - 1)$. According to the averaged results summarized in table 1, we set $\Lambda_0 = 1.7$. This formula gives (1) $\lambda = 0$ for

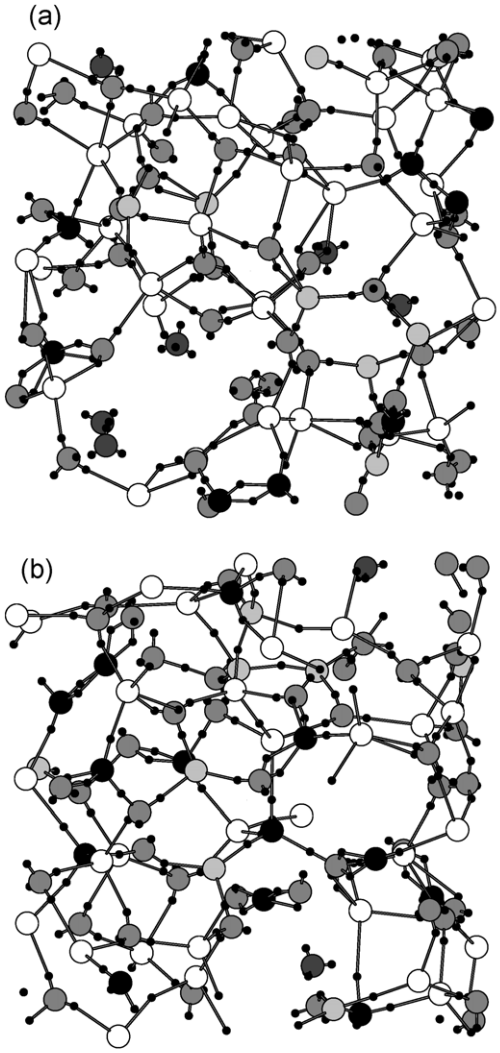

Figure 1. Snapshots from the liquid quench simulations of Si–B–C–N materials with the composition $Si_{31}B_8C_9N_{46}Ar_6$ (panel a) and $Si_{31}B_8C_{13}N_{46}Ar_2$ (panel b). Large black, dark grey (isolated), medium grey, light grey and white circles correspond to C, Ar, N, B and Si, respectively, while the small black dots represent Wannier function centres (WFCs).

purely covalent homonuclear bonds (i.e. with a Wannier centre exactly in the middle of the bond), (2) $\lambda \cong 1$ for bonds between elements from IIIA and VA group and (3) $\lambda \cong 0.4$ for bonds in SiC which is a IVA group material, but partially ionic and often considered (c-SiC) to be a partway between a IV group covalent and a III–V group ionic semiconductor [26].

Table 1 includes exact ionicities of all the bonds with non-negligible populations in a number of simulated Si–B–C–N samples. It was found that behaviour of the atoms is in agreement with their electronegativities and does not depend significantly on sample composition. In particular, the ionicities of homonuclear, heteronuclear single and heteronuclear double bonds are 0.1–0.3, 0.4–1.0 and 1.0–2.0, respectively (note that the homonuclear bonds are not exactly covalent in the disordered amorphous networks). Ionicities

Table 1. The ionicity of bonds in selected crystalline materials (upper part) and in simulated Si–B–C–N materials (lower part) according to Cohen's definition (λ) and to the positions of calculated Wannier function centres (Λ). Bonds with negligible or zero populations in all the samples simulated are not included. In heteronuclear bonds, the WFCs are closer to the atom with minus in superscript.

Material/bond	Bond ionicities	
	Λ	λ
c-SiC	1.32	0
w-SiC	1.28	0
c-BN	1.73	1
w-BN	1.69	1
c-AlP	1.69	1
w-AlN	1.97	1
Si–Si	1.10	0.1
Si^{+}–C^{-}	1.30	0.4
Si^{+}–N^{-}	1.70	1.0
Si^{+}=N^{-}	2.10	1.6
B^{+}–C^{-}	1.40	0.6
B^{+}–N^{-}	1.70	1.0
B^{+}=N^{-}	2.40	2.0
C–C	1.05	0.1
C=C	1.20	0.3
C^{+}–N^{-}	1.30	0.4
C^{+}=N^{-}	1.70	1.0
C^{+}≡N^{-}	1.70	1.0
N–N	1.05	0.1

of all double bonds are higher than ionicities of equivalent single bonds. In accordance with the definition of λ, the single B–N and double B=N bonds (elements from the IIIA and VA group) are the most ionic of all the corresponding single and double bonds, followed closely by the Si–N and Si=N bonds, respectively. The C-containing bonds have relatively low ionicities, but the effect which this should have on increasing bulk modulus will be offset by the high proportion of double and even triple C-containing bonds [27].

Table 2 quantifies the effect of observed structural characteristics on bulk moduli of the studied compositions $Si_{31}B_8C_{13}N_{46}Ar_2$ ($U_b = -100$ V) and $Si_{31}B_8C_9N_{46}Ar_6$ (-500 V). It is shown that the averaged coordination numbers of all atoms, except carbon, increase at the shorter cooling time (lower $|U_b|$ and consequently lower Ar content). The coordination number of carbon is unaffected. The increase is most significant for boron, which correlates with experimentally predicted existence of an energy window for preferential formation of B(sp^3)–N bonds at a low $|U_b|$ in BN [28] and Si–B–C–N [6] materials. As can be seen in table 2, the material prepared with the lower $|U_b|$ value possesses a higher total averaged coordination number and lower averaged bond ionicity (see generally lower ionicities of single bonds in table 1). This would be expected to have a positive effect on its bulk modulus. In contrast, because single bonds are always longer than equivalent double bonds, it can be seen that in the low $|U_b|$ material the averaged bond length is higher. This would be expected to have a negative effect on its bulk modulus. The last row of table 2 shows tha, according to Cohen's formula, individual effects of all discussed structural differences on bulk modulus are up to 3%, and collectively their effect is close to zero. Note that the formula used was developed for a particular class of crystalline material and can therefore

Table 2. The averaged coordination number of the individual atoms, and the total coordination number (without argon), bond length and bond ionicities (Λ and λ), together with their effect on bulk modulus, B_m, determined using Cohen's formula, for simulated Si–B–C–N materials with the composition $Si_{31}B_8C_{13}N_{46}Ar_2$ (deposited at $U_b = -100$ V) and $Si_{31}B_8C_9N_{46}Ar_6$ (deposited at $U_b = -500$ V).

Film composition	Averaged coord. numbers				Total coord. number	Bond length (Å)	Bond ionicities	
	Si	B	C	N			Λ	λ
$Si_{31}B_8C_{13}N_{46}Ar_2$	3.90	3.24	3.03	2.82	3.22	1.7454	1.56	0.80
$Si_{31}B_8C_9N_{46}Ar_6$	3.85	3.10	3.03	2.79	3.18	1.7311	1.64	0.91
					Changes in bulk modulus (%)			
					1.1	−2.9		1.4

provide only a rough guide for amorphous materials. However, it is clear that the calculated structural differences (despite significant differences in cooling times used and in numbers of implanted Ar atoms considered) cannot fully explain the experimentally observed differences in mechanical properties of these materials with similar Si–B–C–N compositions, deposited under different conditions.

3.1.2. Effect of argon implantation. Although there is no method available for a direct calculation of hardness (including possible effects of long timescale crystallization or changes in elemental compositions due to annealing), structural phenomena potentially affecting the hardness can be examined. One of the promising findings is shown in figure 2. It compares segregation of Si atoms around implanted Ar atoms in a sample of composition $Si_{32}B_{10}C_6N_{52}Ar_6$ (panel a) with the hardness of three Si–B–C–N samples of similar compositions after their annealing and cooling down to the room temperature (panel b). All the three samples shown in figure 2(b) were deposited at high (75%) Ar content in a N_2–Ar gas mixture, which led to relatively high contents of implanted Ar atoms. The other deposition conditions were: a $C_{20}Si_{60}B_{20}$ sputter target, $U_b = -100$ V and $T_s = 350\,^{\circ}C$ (squares), $C_5Si_{75}B_{20}$ sputter target, $U_b = -100$ V and $T_s = 350\,^{\circ}C$ (circles), and $C_5Si_{75}B_{20}$ sputter target, $U_s = U_f$ and $T_s \leqslant 250\,^{\circ}C$ (triangles).

As described previously, the segregation of Si around implanted Ar atoms leads to the formation of a sort of two-phase material, consisting of amorphous Si-rich and Si-poor regions [12]. We believe that this can lead to an increase in the extrinsic hardness, in the same way as described recently for mixtures of two nanocrystalline or a nanocrystalline and amorphous structures (see, for example, [29]). It can be seen in figure 2 for all the three samples shown that the 'extra hardness', which the material obtains (or loses) due to the annealing in He, has a similar temperature dependence as the activated segregation of Si around Ar atoms. These results collectively suggest that annealing of the Si–B–C–N materials containing implanted Ar leads to changes in their hardness due to the segregation of Si around the Ar-containing cavities. This increases with temperature up to 1000 K, and then starts to decrease above 1500 K where high kinetic energies start to inhibit a stable segregation [12].

Figure 3 shows the segregation phenomenon in detail for the same pair of samples with different contents of Ar atoms (i.e. $Si_{31}B_8C_{13}N_{46}Ar_2$ and $Si_{31}B_8C_9N_{46}Ar_6$), characterized in table 2. In the sample containing 6 at.% of argon (figure 3(b)), most of the network atoms have at least one implanted Ar atom at a distance of $\leqslant$4.0 Å (upper bound of the first peaks). The limit is slightly higher than 3.6 Å in figure 2, probably due to a different atomic density. In contrast, in the sample containing 2 at.% of argon (figure 3(a)), the distances to the nearest Ar

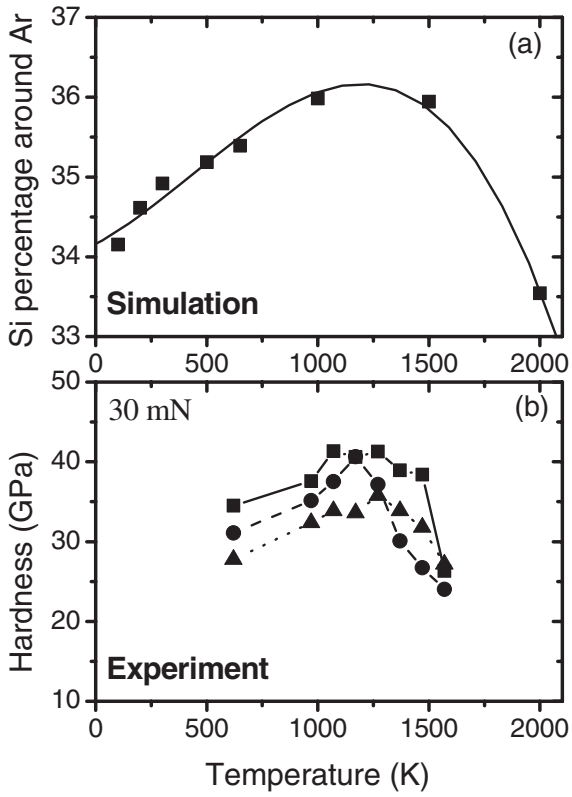

Figure 2. Panel (a), adapted from [12], shows segregation of Si atoms around implanted Ar atoms in samples with the composition $Si_{32}B_{10}C_6N_{52}Ar_6$ equilibrated at various temperatures. The vertical axis refers to the percentage of the Si atoms in the group of Si, B, C and N atoms that lie in the vicinity ($\leqslant$3.6 Å) of an Ar atom. Panel (b) shows hardness of three Si–B–C–N films with similar compositions as the simulated one, measured after annealing in helium and cooling back to the room temperature, as a function of the annealing temperature.

atom span a wide range with most distributions showing several comparable peaks up to the maximum possible distance imposed by the periodic simulation cell.

We define the Si-rich regions (in a close proximity to Ar atoms) as those which consist of the atoms in the first peaks in figure 3. They fill a space between two concentric spheres with the radii of 2.5 and 4.0 Å around each implanted Ar atom. The space around each Ar atom up to approximately 2.5 Å is empty according to figure 3. The spheres can, of course, intersect especially at a high Ar content. The rest of the sample constitutes the Si-poor matrix (away from the Ar atoms). In the 6% Ar sample, most of the constituent atoms are included in the high-Si regions in close proximity to Ar due to a sufficiently high concentration of the Ar atoms. Therefore the Si content cannot be increased very much in these regions. This results in an almost homogeneous material. In the 2% Ar sample, the Ar density is low enough to allow segregation of the constituent atoms into the Si-rich regions (close to the Ar atoms) and Si-poor regions (far from the Ar atoms). The proportions of these two different composition zones are fairly balanced, suggesting the formation of a true heterogeneous material.

The ideas presented in figure 3 are quantified in table 3. It is seen that in the 2% Ar sample, comparable numbers of all network atoms are included in the close-to-Ar and far-from-

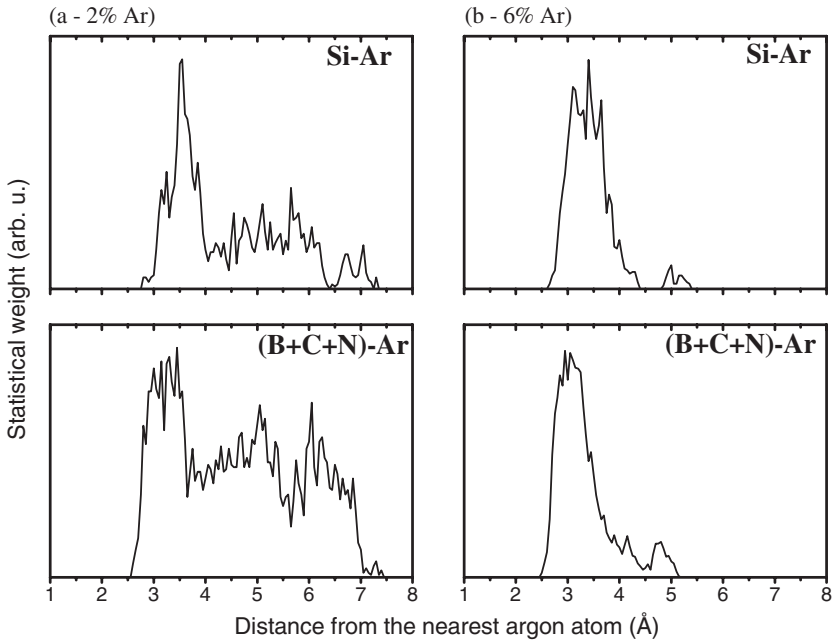

Figure 3. Distributions of the distances of Si, B, C and N atoms to the nearest Ar atom in samples with the composition $Si_{31}B_8C_{13}N_{46}Ar_2$ (a) and $Si_{31}B_8C_9N_{46}Ar_6$ (b). Data are summed over all atoms of the respective element and over the 69 snapshots made during a 0.5 ps production run at the end of the liquid quench simulation. In the latter sample, most of the atoms are close to at least one Ar atom. In the Si–Ar distributions, relatively more of the distances are in the lower part of the range.

Table 3. The elemental composition and relative size (in proportion of atoms included) of the regions resulting from segregation of Si atoms in the vicinity of implanted Ar atoms in the $Si_{31}B_8C_{13}N_{46}Ar_2$ and $Si_{31}B_8C_9N_{46}Ar_6$ structures. Atoms in the vicinity of an Ar atom are defined to be those which are closer than 4 Å to an Ar atom.

Film composition	Composition of regions	Fraction of atoms (%)
$Si_{31}B_8C_{13}N_{46}Ar_2$	Around Ar: $Si_{37}B_{10}C_9N_{44}$	41.7
	Rest: $Si_{28}B_7C_{16}N_{49}$	58.3
$Si_{31}B_8C_9N_{46}Ar_6$	Around Ar: $Si_{34}B_8C_{10}N_{48}$	90.1
	Rest: $Si_{22}B_{12}C_{10}N_{56}$	9.9

Ar zones (42 and 58%, respectively). The Si enrichment around the Ar atoms is consequently relatively high in comparison with the other sample. In contrast, in the 6% Ar sample, 90% of all the network atoms are included in the close-to-Ar zones. The Si enrichment is therefore relatively low there, despite a significant reduction of the Si content in the far-from-Ar rest of the sample. Assuming that (1) the hardness of a mixture of nanograins of two materials is at their proper ratio higher than the hardnesses of both constituents even when they are significantly different [29], and that (2) the hardness dependence of the mixture of the Si-rich and Si-poor regions on their volume ratio is roughly symmetrical, the 0.42 to 0.58 ratio calculated for the 2% Ar material leads to a significantly higher extrinsic hardness than the 0.90–0.10 ratio calculated for the 6% Ar material.

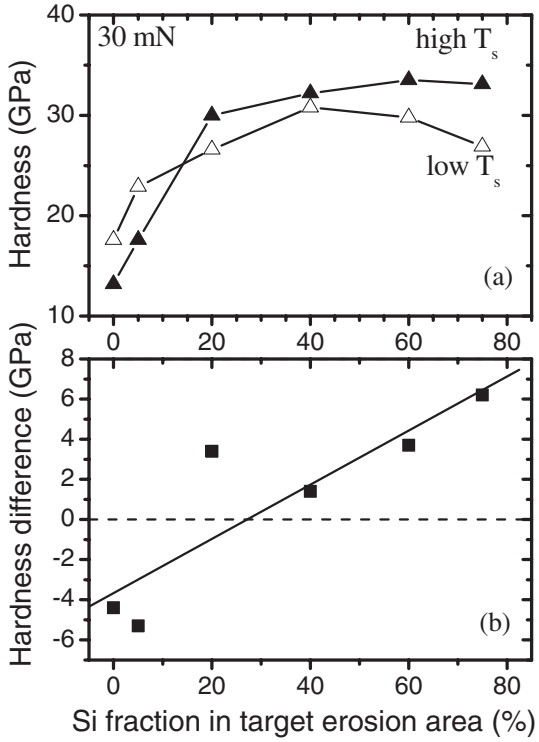

Figure 4. Panel (a) shows hardness of the Si–B–C–N films samples deposited using a B_4C–Si sputter target in a 25% N_2 + 75% Ar gas mixture at substrate temperatures $T_s = 700\,^{\circ}C$ (high T_s—full symbols) and low $T_s \leqslant 250\,^{\circ}C$ (high T_s—empty symbols), and a substrate bias voltage $U_b = -100$ V. Panel (b) shows differences between the corresponding hardness values presented in panel (a). The line is a fit from linear regression.

3.2. Supporting experimental results

The conclusion concerning the effect of the implanted Ar atoms and the segregation of Si atoms around them on hardness is examined in the light of two additional experimental results. These results show that both the silicon content (figure 4) and the argon content (figure 5) in the Si–B–C–N materials are important for their hardening.

Figure 4 shows the effect of deposition temperature on film hardness at various sputter target compositions. Two series of the (Si)–B–C–N samples were deposited using a B_4C–Si target at the substrate temperatures $T_s = 700\,^{\circ}C$ and $T_s \leqslant 250\,^{\circ}C$ (no ohmic heating). The other deposition conditions were a 25% N_2 + 75% Ar gas mixture and $U_b = -100$ V for all samples in these series, leading to 2 at.% of implanted Ar [5]. Absolute values of the film hardness are presented in figure 4(a), and the corresponding hardness differences caused by increase in T_s from less than 250 to 700 °C (probably overestimated for 20% Si) are shown in figure 4(b). It can be seen that, while this difference is negative (that is, the films deposited at the lower T_s are harder) at zero or low Si fractions in target erosion area, it increases almost linearly with an increasing Si fraction in the target erosion area over the whole range observed, becoming positive when the Si fraction is above ∼30%. The slope of the increase is approximately 0.3 MPa/1 °C of the substrate temperature and 1% of Si in the target erosion area.

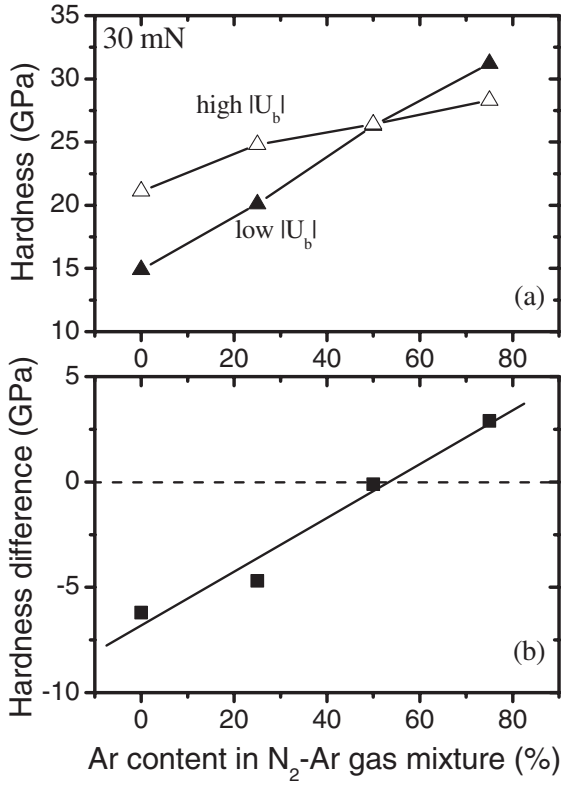

Figure 5. Panel (a) shows hardness of the Si–B–C–N films deposited using a B_4C–Si sputter target with a fixed 75% Si fraction in the erosion area at substrate bias voltages $U_b = -100$ V (low $|U_b|$—full symbols) and $U_b = -500$ V (high $|U_b|$—empty symbols), and a substrate temperature $T_s = 350\,^{\circ}C$. Panel (b) shows differences between the corresponding hardness values presented in panel (a). The line is a fit from linear regression.

The results in figure 4 can be understood taking into account that the physical processes determining hardness are different for films with a low Si content compared to those with a high Si content. In the former case, the compressive stress caused by implanted Ar atoms cannot be relaxed by segregation of Si around them [12]. Such films deposited at low temperatures exhibit a higher compressive stress leading to higher values of hardness. The intrinsic stress can be relieved by atomic rearrangement if the deposition is carried out at an elevated temperature ($T_s = 700\,^{\circ}C$). With the increasing Si content in materials, the thermally activated stress relaxation becomes less important because the compressive stress caused by the implanted Ar atoms is relieved by segregation of Si around them [12]. The main process increasing material hardness at high Si contents is therefore the segregation of the constituent atoms into nanoscale regions of two phases. This thermally activated process is naturally more significant at higher T_s (up to ∼1000 K, see figure 2) and at higher Si content in materials. It leads to an increase in hardness with the deposition temperature at high Si contents.

Figure 5 shows the film hardness as a function of the Ar content in the gas mixture for two series of the Si–B–C–N films. They were deposited using a $(B_4C)_{25}Si_{75}$ sputter target at the substrate bias voltages $U_b = -100$ and -500 V, and the substrate temperature $T_s = 350\,^{\circ}C$. Absolute values of the hardness are presented in figure 5(a), and the corresponding hardness

differences caused by a change in U_b from -500 to -100 V are shown in figure 5(b). It can be seen that, while this difference is negative (that is, the films deposited at $U_b = -500$ V are harder) at zero or low Ar fractions in the gas mixture, it increases almost linearly with an increasing Ar fraction in the gas mixture over the whole range observed, being positive at the 25% N_2 + 75% Ar gas mixture composition. The slope of the increase is approximately 0.3 MPa/1 V of the substrate bias voltage and 1% of Ar in the gas mixture.

The results in figure 5(a) can be understood taking into account that the physical processes affecting material hardness are different at zero and at high Ar contents in the gas mixture (resulting in Ar implantation into deposited materials). In the former case, the hardness is higher for the materials deposited at $U_b = -500$ V, possibly due to a stronger bombardment by nitrogen ions which leads to ion-induced knock-on subplantation of film-forming particles, resulting in densification of the deposited materials. The same behaviour was observed also for other amorphous films, such as CN_x [30], prepared in a pure N_2. As can be seen in figure 5, the successive increase of the material hardness with an increasing Ar fraction in the gas mixture is much more pronounced at $U_b = -100$ V. Thus films deposited with a high Ar fraction in the gas mixture have a higher hardness at $U_b = -100$ V. Our simulations indicate that the level of Ar incorporation in the films at $U_b = -500$ V is too high to allow substantial Si segregation. An optimum segregation is facilitated for a low (around 2%) Ar incorporation as found in the films deposited with at $U_b = -100$ V. Also the fact that this phenomenon was not observed for B–C–N materials supports the idea that the segregation of Si around Ar atoms is responsible for the hardness enhancement in this case.

4. Conclusions

A method to calculate the bond ionicities, λ, using Wannier function centres was developed. Typical values were 0.1–0.3 for homonuclear bonds, 0.4–1.0 for heteronuclear single bonds and 1.0–2.0 for heteronuclear double bonds. A simulated sample deposited at a low substrate bias voltage $U_b = -100$ V possessed a higher averaged total coordination number at a lower bond ionicity and higher bond lengths than the equivalent high $|U_b|$ simulated structure ($U_b = -500$ V). Quantitatively, differences in these quantities alone cannot explain the experimentally observed differences in mechanical properties of these samples with similar Si–B–C–N compositions. Structures of the samples deposited in an Ar-containing gas mixture at various U_b values were examined by simulations. Analysis of the simulation results was focused on the formation of Si-rich regions around implanted Ar atoms. It was found that the 6% Ar sample ($U_b = -500$ V) is not far from homogeneous (most of the network atoms are close to at least one Ar), while the 2% Ar sample ($U_b = -100$ V) is heterogeneous, with similar volumes of the Si-rich regions close to the Ar atoms and Si-poor regions far from the Ar atoms. This may lead to a higher extrinsic hardness of the material deposited at the lower $|U_b|$. The prediction was successfully tested against several experimental results.

Acknowledgments

This work was supported by the Ministry of Education of the Czech Republic through Project No. MSM 4977751302, and by the Metacentrum Czech Republic.

References

[1] Riedel R, Kienzle A, Dressler W, Ruwisch L, Bill J and Aldinger F 1996 *Nature* **386** 796
[2] Müller A, Gerstel P, Weinmann M, Bill J and Aldinger F 2000 *J. Eur. Ceram. Soc.* **20** 2655

[3] Houška J, Vlček J, Hřeben S, Bilek M M M and McKenzie D R 2006 *Europhys. Lett.* **76** 512
[4] Jungermann H and Jansen M 1999 *Mater. Res. Innov.* **2** 200
[5] Vlček J, Potocký S, Čížek J, Houška J, Kormunda M, Zeman P, Peřina V, Zemek J, Setsuhara Y and Konuma S 2005 *J. Vac. Sci. Technol.* A **23** 1513
[6] Houška J, Vlček J, Potocký S and Peřina V 2007 *Diamond Relat. Mater.* **16** 29
[7] Ramakrishnan P A, Wang Y T, Balzar D, An L, Haluschka C, Riedel R and Hermann A M 2001 *Appl. Phys. Lett.* **78** 3076
[8] Rooke M A and Sherwood P M A 1997 *Chem. Mater.* **9** 285
[9] Hegemann D, Riedel R and Oehr C 1999 *Chem. Vapor Depos.* **5** 61
[10] Lu L, Song Y C and Feng C X 1997 *J. Mater. Sci. Lett.* **17** 599
[11] Vlček J, Potocky S, Houska J, Zeman P, Perina V and Setsuhara Y 2006 *Trans. Mater. Res. Soc. Japan* **31** 447
[12] Houska J, Warschkow O, Bilek M M M, McKenzie D R, Vlcek J and Potocky S 2006 *J. Phys.: Condens. Matter* **18** 2337
[13] McCulloch D G, McKenzie D R and Goringe C M 2000 *J. Appl. Phys.* **88** 5028
[14] Fitzhenry P, Bilek M M M, Marks N A, Cooper N C and McKenzie D R 2003 *J. Phys.: Condens. Matter* **15** 165
[15] Hohenberg P and Kohn W 1964 *Phys. Rev.* B **136** 864
[16] Kohn W and Sham L 1965 *Phys. Rev.* A **140** 1133
[17] CPMD, Copyright IBM Corp 1990–2006 Copyright MPI fur Festkörperförschung Stuttgart 1997–2001
[18] Goedecker S, Teter M and Hutter J 1996 *Phys. Rev.* B **54** 1703
[19] Becke A D 1988 *Phys. Rev.* A **38** 3098
[20] Lee C, Yang W and Parr R G 1988 *Phys. Rev.* B **37** 785
[21] Houška J, Bilek M M M, Warschkow O, McKenzie D R and Vlček J 2005 *Phys. Rev.* B **72** 054204
[22] Marks N A 1997 *Phys. Rev.* B **56** 2441
[23] McCulloch D G, McKenzie D R and Goringe C M 2000 *Phys. Rev.* B **61** 2349
[24] Vlček J, Rusňák K, Hájek V and Martinů L 1999 *J. Appl. Phys.* **86** 3646
[25] Resta R 1998 *Phys. Rev. Lett.* **80** 1800
[26] Cohen M L 1985 *Phys. Rev.* B **32** 7988
[27] Houška J, Čapek J, Vlček J, Bilek M M M and McKenzie D R 2007 *J. Vac. Sci. Technol.* A submitted
[28] Panayiotatos Y, Logothetidis S, Handrea M and Kautek W 2003 *Diamond Relat. Mater.* **12** 1151
[29] Musil J 2000 *Surf. Coat. Technol.* **125** 322
[30] Hájek V, Rusňák K, Vlček J, Martinů L and Gujrathi S C 1999 *J. Vac. Sci. Technol.* A **19** 899